Ocean Remote Sensing: Concept to Realization for Physical Oceanographic Studies

Tapan Misra, Rashmi Sharma, Raj Kumar, and Pradip K. Pal

Abstract In this chapter, we briefly describe various space-borne sensors which have become the backbone of oceanographic research and applications. Operating in the electromagnetic region (mainly optical to microwave), these sensors provide measurements of various physical oceanographic parameters such as sea surface temperature, height, salinity, wave, winds, sea ice extent, thickness, and concentration on a global scale. This chapter also describes remote sensing techniques, measurement principles, retrieval of geophysical parameters, and their applications.

1 Introduction

Remote sensing by space-borne sensors has become an extremely important component of ocean observing system. Major programs like Global Ocean Data Assimilation (GODAE) and GODAE OceanView have established the role of satellites in observing oceans for research and operational needs. The vast expanse of ocean presents a formidable task to be studied at many scales using in-situ measurements by ships, buoys, and floats. Space-borne sensors provide repetitive measurements with synoptic view at a glance. Satellite Oceanography encompasses oceanographic research and technological development resulting from systems in Earth's orbit. Remote sensing technology makes use of electromagnetic (*em*) radiations of certain wavelength (ranging from visible to microwave) to distinguish different objects. Satellite observations are based on measurements of energy either emitted from earth and atmosphere (*passive sensing*) or returned as backscatter from earth–atmosphere system when a satellite-based pulse source illuminates (*active sensing*) the target. The absorption by atmospheric gases and reflection/emission from the earth's surface is the backbone of these remote sensing methods. Oceanographic parameters observed and measured by space-borne sensors are sea surface winds, sea surface temperature (SST), ocean surface waves, sea surface

T. Misra • R. Sharma (✉) • R. Kumar • P.K. Pal
Space Applications Centre, Ahmedabad, India
e-mail: rashmi@sac.isro.gov.in

salinity, sea surface height, and ocean color. Solar radiation reflected/scattered from the ocean surface mainly relates to ocean color measurements, and thermal infrared (*IR*) emitted from the surface provides information about SST. While emitted microwave radiation is related to both temperature and roughness of the sea, backscattered energy from the surface provides measurements of roughness, slope, and height of the sea surface. Oceanographic parameters are estimated by suitable retrieval algorithms utilizing the underlying physics of the process of observations. Due to this, it needs detailed calibration and validation, prior to the estimation of the parameters. Processes of interest in the ocean span a horizontal length scale ranging from 1 mm to 1000 km, and a timescale ranging from seconds to years. Observations of such wide ranges must necessarily employ a variety of experimental strategies in terms of wavelength selection and space–time sampling.

Satellite Oceanography began with the launch of first artificial satellite Sputnik-1 by the USSR in 1957. Since then, in the last 60 years, spectacular advances have been made in this field. First civilian oceanographic satellite, SEASAT, was launched by NASA in the year 1978. The satellite carried radar altimeter, scatterometer, visible and infrared radiometer, microwave radiometer, and synthetic aperture radar to monitor oceans. Although this mission lasted only for 105 days, it provided immensely valuable data to understand oceans and their role in climate. India's tryst with meteorological and oceanographic satellites started with the launch of its first experimental remote sensing satellite, Bhaskara-1, in the year 1979. IRS–P3 (launched in March 1996) with the sensor MOS onboard and IRS–P4 (or Oceansat-1, launched in May 1999) with multifrequency scanning microwave radiometer (MSMR) and ocean colour monitor (OCM) payloads gave significant fillip to these activities in terms of real-time utilization of satellite-based geophysical information and enhanced user interactions. There are a large number of ocean optical and microwave instruments on the anvil in international arena – assuring uninterrupted supply of data for ocean studies. ISRO's own missions, viz. Oceansat-2, RISAT, INSAT–3D, Megha Tropiques, and SARAL/AltiKa have contributed significantly towards the understanding of oceans.

The book by Robinson [57] gives basic concepts of ocean remote sensing in greater detail. Hence, in this chapter, we provide a brief account of satellite technologies, sensors, and applications, with suitable examples wherever possible from satellites launched in the recent past.

2   Remote Sensing of Sea Surface Temperature

Sea surface temperature (SST) is one of the first oceanographic parameters to be measured from the space and is widely used by the ocean and climate researchers. SST can be measured from both Infrared (IR) and passive microwave radiometers, each with its own advantages and drawbacks. The SST varies on diurnal, seasonal, interannual, and on climate scale. Diurnal variability in SST has been observed up to 6°C [23]. The first global composite of SST from the satellite measurements was

prepared in 1970s [42]. Since then numerous satellites have been launched for the measurement of SST by several space agencies.

2.1 Measurement Principle: Thermal IR and Microwave Regime

Radiometers which can be imaging or non-imaging are passive sensors that operate in the visible, infrared, and microwave regions of *electromagnetic spectrum*. These radiometers detect naturally emitted or reflected radiation from the earth's surface. Thermal emission and absorption from atmospheric constituents mainly contribute to the *em* energy in the thermal *IR* and microwave regions, whereas in the visible and near *IR* range it is the reflection/scattering of the incident solar radiation which is prominent. That is why the satellite measurements in the spectral bands within the visible region are sensitive to the reflectance/absorption properties of water constituents over oceanic regions, whereas in the infrared/microwave region, it is sensitive to the emission/absorption from the ocean surface as well as the atmospheric constituents. Reflectance of seawater is sensitive to the surface roughness, bathymetry, and presence of tracers such as salinity, chlorophyll, turbidity, etc.

The basic principle behind the passive radiometry is Planck's law which describes a relationship between thermal emission and the physical temperature of an ideal blackbody (with emissivity as unity):

$$L_\lambda = \frac{2hc^2}{\lambda^5 \left(e^{hc/\lambda kT} - 1 \right)}$$

where h is Planck's constant and k is Boltzmann's constant.

The relationship between the wavelength at which a blackbody emits the maximum radiation, λ_{max}, and the physical temperature of the blackbody, *T*, is given by Wein's displacement law (i.e., $\lambda_{max} T$ = constant). At larger wavelengths, that is in the microwave region (1–40 GHz), Planck's law becomes the Raleigh-Jean approximation which states that the emitted radiation is directly proportional to the temperature of the emitting surface. The above relation is much simpler for microwave than the one for *IR* radiometry where the full Planck function must be used. For this reason, emitted radiation is sometimes simply referred to as the brightness temperature.

Since the aim of the radiometer is to measure the SST, a suitable spectral band is chosen such that the atmospheric attenuation is minimum and there is sufficiently large amount of energy received at the satellite sensor. These spectral bands in the electromagnetic spectrum are known as the atmospheric windows. There are two important atmospheric windows in the infrared spectrum, 3.8 μm midwave infrared (MWIR) window and 10–12 μm longwave or thermal *IR* (LWIR or TIR) window that are used for the SST retrieval. The peak of the emitted radiation from the sea surface having SST around 300 K is in the wavelength range 10–12 μm which is a

window region. This allows to obtaining high spatial resolution SST with highest accuracy. On the other hand, the MWIR window has the advantage in terms of maximum sensitivity of the observed radiances with respect to the changes in the surface temperature due to shorter wavelengths. In the microwave region, the window region exists below 18 GHz where there is significantly smaller attenuation due to atmosphere even in the presence of the cloud. However, due to the longer wavelengths the sensitivity of the microwave radiometer observations to the changes in the surface temperature is smaller than that in the infrared. In addition to this, a small amount of radiated energy in this region of the *em* spectrum causes a large noise equivalent ΔT (NEΔT) which necessitates a coarser spatial resolution or larger antenna to obtain a meaningful signal for the SST retrieval. The C-band (4–8 GHz) in the microwave spectrum is best suited for the SST retrieval due to its higher sensitivity and lower impact due to variable wind-induced surface roughness as well as other atmospheric attenuations. Keeping in mind the advantages they provide in the infrared and microwave parts of the *em* spectrum, a blended product is possible by suitably combining the best features of both the sensors.

2.2   *Retrieval of Geophysical Parameters*

We first start with the SST retrieval from radiances measured in the infrared region of the *em* spectrum. For SST retrieval, mainly the atmospheric windows in the MWIR (3.8–4 µm) and LWIR (10–12 µm) are used. However, due to the contamination of the emitted radiation by the reflected solar radiation in the MWIR band during daytime, this band is used to retrieve SST only during nighttime, hence the name given to it as the nighttime SST channel. During daytime, the LWIR window channels are used for SST retrieval. However, absorption in this band due to highly variable atmospheric water vapor makes SST retrieval erroneous. To correct for the water vapor absorption, the split window channels (i.e., 10.3–11.3 µm or T_{11} and 11.5–12.5 µm or T_{12}) observations are employed. Absorption in the second split window channel is higher than the first channel; therefore, the difference of brightness temperature observations in these two channels gives a quantitative estimate of the atmospheric water vapor that is required for correction in the SST computation. Due to the weak water vapor absorption in these split window channels, the weighting function for these channels lies very close to the surface. Therefore, the amount of water vapor estimated from their differences is equivalent to the total column water vapor as more than 90% of the water vapor lies in the lowest few kilometers of the atmosphere.

A simple form of the dual channel algorithm is given as follows:

$$SST = A_1 T_{11} + A_2 T_{12} + \left[A_3 \left(T_{11} - T_{12} \right) + A_4 \right] \sec \theta + A_5$$

where A_1, A_2, A_3, A_4, and A_5 are coefficients derived using regression analysis between actual SST and the collocated satellite observations. Since water vapor

absorption is strongly dependent on the observation zenith angle (θ), the relation needs correction for the zenith angle variation. The MWIR channel at 3.8 μm is highly sensitive to the surface temperature variations; so, this channel can replace T_{11} during nighttime when contamination from reflected solar radiation is absent. During nighttime, this channel along with the split window channels provides the accurate SST retrieval.

Passive microwave radiometer measurements of the sea surface from space functions in essentially the same way as do the infrared radiometers. Normally operating at electromagnetic radiation between 1 and 200 GHz frequencies, these radiometers observe the thermal radiation emitted in the microwave part of the spectrum by the sea surface, atmosphere, and that reflected by the sea surface. At these comparatively longer wavelengths, there is no scattering by the atmosphere or aerosols, haze, dust, or small water particles in the clouds. This provides all weather-sensing capability from a microwave sensor, although liquid water in the form of precipitation does scatter the radiation and can render the atmosphere opaque at microwave frequencies. On the other hand, there are certain disadvantages of the microwave sensors. The emitted radiation is very weak at these wavelengths, which leads to poor signal-to-noise ratio (SNR). To improve the SNR, emission from a larger field of view must be viewed which leads to the coarser spatial resolution. Another aspect is that emissivity of the sea at microwave frequencies is also very small and varies with the dielectric properties of seawater and the surface roughness. Since the dielectric constant varies with temperature, salinity, and frequency, the observations by a multichannel microwave radiometer must contain information not only about the sea surface temperature, but also about the ocean salinity and the sea state. Theoretically, 6 GHz is considered as the best frequency for SST because of the sensitivity of brightness temperature to the changes in SST peaks at this frequency with low sensitivity to both salinity as well as surface roughness (Fig. 1). A frequency of 10 GHz is also considered suitable for SST where there is adequate sensitivity for SST with the added advantage of better spatial resolution. Examples of passive microwave radiometer providing SST estimations are Nimbus SMMR, Oceansat-1 MSMR, TRMM TMI, Aqua AMSR, and NPP ATMS. A typical algorithm for retrieval of SST from microwave radiometer observations makes use of multichannel observations to correct for sea surface roughness, atmospheric water vapor, cloud liquid water, etc., and has the following form:

$$SST = A_1.T_{6H} + A_2.T_{6V} + A_3.T_{10H} + A_4.T_{10V} + A_5.T_{18H}$$
$$+ A_6.T_{18V} + A_7.T_{21H} + A_8.T_{21V} + A_9$$

where A_{1-9} are coefficients derived empirically, and T_{nH} and T_{nV} are H and V polarization brightness temperatures at frequency, $n = 6, 10, 18, 21$ GHz. In this relation, 6 GHz is the primary channel for SST retrieval, whereas 10 GHz provides the correction term for the wind-induced variable emissivity, and difference in the 18 and 21 GHz provides the correction term for the total column water vapor.
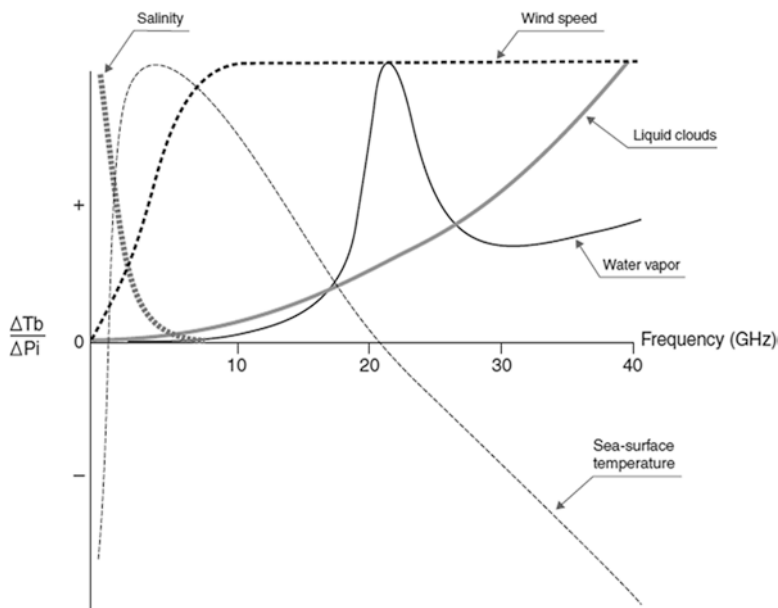
Fig. 1 Relative sensitivity of brightness temperature observation for various oceanic parameters as a function of microwave radiometer frequency (Source: Original figure by Thomas T. Wilheit, NASA/GSFC)

2.3   Accuracy, Precision, and Sampling

IR-based methods provides the best-quality and high spatial resolution SST with an accuracy better than 0.3 K. Typical resolution of SST from such sensors is ~1–4 km. However, SST measurement from IR sensors is limited to the clear sky conditions. This is a major drawback as far as getting SST from IR sensors is concerned, especially in the regions largely dominated by the clouds. For Indian Ocean region, specifically the Bay of Bengal, IR sensors are mainly useful during winter time when the sky conditions are largely clear.

In the current scenario, both polar orbiting and geostationary satellites have capabilities to measure SST. In fact, the currently existing geostationary satellites (GOES-E/W, Himawari-8/9, INSAT-3D/3DR, and Meteosat second generation series) are able to provide a global coverage of SST at a temporal resolution better than 30 min. MODIS which is onboard Aqua and Terra satellites has been continuously providing global coverage of SST at ~1 km resolution for more than 10 years. NOAA/AVHRR series of satellites have significantly contributed to the operational and research communities for more than 30 years as pathfinder AVHRR SST. Microwave sensors provide all weather SST measurements. However, the errors are large and the spatial resolution is coarse (~25 km) as compared to the IR sensors. Typical errors from microwave sensors range from 0.5 to 0.8 K. Microwave imager onboard tropical rainfall measuring mission (TRMM/TMI) provided almost

18 years of continuous data of SST in the tropics (±40° latitude belt). It was the most reliable source of SST from microwave sensor in all weather conditions (barring under high winds and rain conditions). Global maps of 3-day running-averaged SST from TMI at a resolution of 25 km are available from 1997 to 2014. Other instruments like AMSR onboard GCOM series and MWI onboard HY-2 series are also in operation providing microwave SST measurements ensuring the continuity.

2.4 Applications of Sea Surface Temperature

SST is a key "boundary forcing" to the atmosphere in the numerical weather prediction models and has a great influence on seasonal, interannual and to some extent on decadal predictions. Satellite-derived SST are assimilated in the ocean models for generating accurate ocean state forecasts. SST is the key variable in the air-sea interaction processes. High-resolution SST is quite useful in the determination of fine-scale horizontal thermal gradients or fronts (Fig. 2). These fine-scale structures can lead to the vertical movement of the biomass nutrients and, therefore, have a potential application in the fishery industry. Thermal fronts also modify the air-sea interaction processes significantly through heat flux exchange. This alteration in the air-sea interaction sometimes can even change the cyclone track [72]. Accurate and well-calibrated SST records are extremely useful for monitoring long-term temperature change and are pointers of climate change. SST fields help in detecting eddies and upwelling regions in the ocean, which are extremely useful for delineating potential fishing zones.

2.5 New Frontier in SST Measurements

There has been a tremendous improvement in the synergistic use of passive microwave and infrared sensors for providing continuous global high-resolution SST images for operational and research use. The Group of High Resolution SST (GHRSST [16]) is a merged product comprising of SST observations from several existing microwave and infrared sensors. Researchers involved in generating GHRSST are providing SST products on a near-real time basis for its use in the operational weather forecasting and in ocean process studies. The GHRSST program has resulted in the growth of data streams from all across the globe and has provided SST with common data format along with uncertainty estimates. All these efforts have led not only to the creation of long-term climate data records using existing satellite sensors, but also to the development of a procedure to provide a flawless integration of new satellite sensors.

Geostationary satellites can be quite crucial for providing synoptic measurements of SST at very high sampling frequencies. Efforts are on to increase the sampling rate up to 10 min interval so as to provide high frequency variability
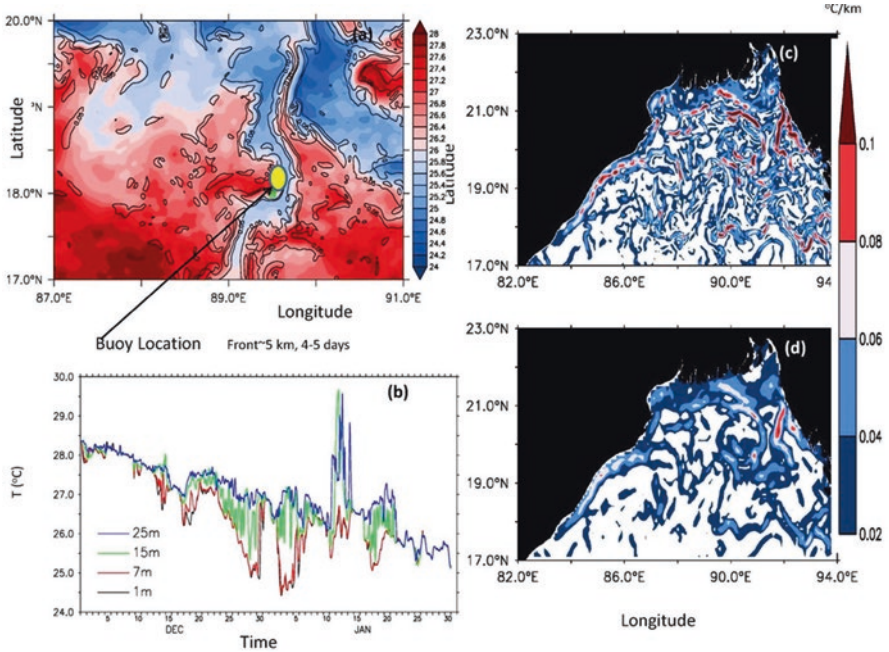
Fig. 2 Thermal fronts can be seen in the northern BoB from a composite satellite SST image (**a**), and time series of near-surface temperature at four different depths from a buoy at 18ºN, 89.5ºE (**b**). Horizontal SST gradient magnitude (°C/km) for January 15, 2013. The estimated temperature gradients based on 1 km resolution (**c**) and 10 km resolution (**d**) (Figure adopted from Wijesekera et al. [68], BAMS: doi: https://doi.org/10.1175/BAMS-D-14-00197.1)

of SST under cloud-free conditions. Himawari-8/9 of Japan Meteorological Agency, GOES-R of NOAA and Meteosat of Eumetsat are providing SST at high temporal sampling. GISAT of ISRO to be launched in a couple of years' time which will be giving SST from geostationary platform at 1 km resolution at 10 min interval.

It is very important to have continuity in the missions to get maximum benefits in operational oceanography services and to have long uninterrupted time series of data for climate studies. Operational continuity of microwave-based SST measurements is of utmost importance for all weather coverage. Future mission of ESA's microwat [54] is also being discussed. Efforts on ground truth collection are also needed to fine-tune the retrieval algorithms. Coastal observations from satellites have always been a challenge due to sudden transition of brightness temperature from land to sea; so, efforts must be towards building a methodology to address these concerns as coastal processes are of extreme importance. He et al. [35] have generated cloud-free daily SST product for West Florida Shelf at a 5-km spatial resolution by optimally combining microwave and infrared measurements.

3 Satellite Altimetry: A Versatile Tool for Ocean Applications

Satellite altimeter is undoubtedly one of the most versatile space-borne instruments for measuring ocean variables. With the primary application of altimetry in understanding the ocean dynamics by making use of sea surface height (SSH) information, it has come a long way where it is unthinkable of getting the estimate of global sea level rise without this instrument. Other ocean variables such as, significant wave height (SWH) and wind speed, are also retrieved from this instrument. These variables are contributing significantly to the operational oceanography.

3.1 History of Satellite Altimetry

Satellite altimeter has a very rich history. The first multipurpose microwave instrument onboard Skylab in 1974 and GEOS-3 (first dedicated altimeter mission) in the following year were more of technology demonstration. Seasat launched by NASA in the year 1978 in its 3-month lifetime demonstrated that altimeter could successfully detect mesoscale eddies. Launched in 1985, Geosat data was used to monitor eddy variability and also marine geoid. These altimeters were the first generation altimeters. Then came more sophisticated dual frequency altimeters (to take care of ionospheric effects) with onboard radiometer and improved orbit determination. First in this class was ERS-1 (1991) launched by European Space Agency, followed by US/French TOPEX/Poseidon (T/P) in 1992. Later a strategy was adopted [41] to observe ocean circulation with scales ranging from mesoscale to large-scale. It was recommended to have low-inclination altimetric mission having a high-accuracy altimeter (reference mission) on a non-sun-synchronous orbit for determining large-scale ocean currents and complementary higher inclination, sun-synchronous altimeter missions that can provide information on mesoscale eddies. This strategy was realized by NASA and CNES with the launch of Jason-1 in 2001 as a reference mission and Envisat launched in 2002 in a higher inclination. And then followed Jason-2/3 and Geosat follow-on missions. Another shift in altimetric measurements came with the launch of ISRO-CNES SARAL/AltiKa mission in the year 2013, which was a gap-filler between Envisat and Sentinel-3 [66]. The SARAL/AltiKa mission was launched at the behest of the international oceanographic community (Ocean Surface Topography-Science Team).

3.2 Measurement Principles

Altimeter is a nadir-viewing radar that transmits short pulses, typically of a few nanoseconds duration, and detects the return pulse along with the two-way travel time. The shape of the return pulse, known as "waveform," represents the time

evolution of the reflected pulse from the footprint of the altimeter. As the name signifies, the primary goal of an altimeter mission is to measure the altitude of the sea surface from a reference ellipsoid. By measuring the two-way travel time of the radar pulse and knowing the speed of the electromagnetic wave, altimeter height above the sea surface called as "range" is computed. Making use of precise orbit determination, the height of the satellite above a reference ellipsoid is obtained. From these two measurements, one can then easily compute the sea surface height (SSH), height with respect to reference ellipsoid, by subtracting the range from the orbit of the satellite (Fig. 3). However, because of the slowing down of the radar pulse during its passage through ionosphere, and atmosphere, several corrections have to be applied. Apart from atmospheric corrections, one needs to correct for sea-state bias and skewness effects. A typical waveform from altimeter over the open ocean is shown in Fig. 4c (upper panel, an example from SARAL/AltiKa). Apart from SSH, one also gets significant wave height (SWH), related approximately inversely to the slope of the leading edge of the reflected pulse or the waveform. The third quantity of interest is ocean surface wind speed, which is empirically related to the maximum backscattered power. Over the ocean, observations are averaged over 1 s giving the along-track resolution of nearly 7 km (varies with ocean wave conditions) and cross-track separation of 40–300 km, depending upon the repeat cycle of the satellite. For altimeters, footprint is determined by the pulse-limited (duration of the pulse) geometry rather than beam-limited geometry. All these details and more on pulse compression method to achieve better range accuracy are described in the work by Chelton et al. [15].

3.3   Retrieval of Geophysical Parameters (Sea Surface Height, Significant Wave Height, and Wind Speed)

In the open ocean, the altimetric echo follows a standard shape, with steeply rising leading edge followed by a trailing edge with gradually diminishing power. This standard shape is in agreement with the theoretical Brown model [8] and hence can be modeled. Though details of the theoretical framework of the radar returns from the ocean surface are given by Brown [8], for the sake of brevity, it is once again briefed here.

Radar return pulse $W(t)$ is a convolution of three terms: (a) the flat sea surface response (FSSR); (b) the sea surface elevation probability distribution function (PDF); and (c) the radar system point target response (PTR) (transmitted pulse as affected by the receiver bandwidth). The first term (a) includes the effects of antenna beam width and the off-nadir pointing angle. The mean return waveform as a function of time t (generally measured in nanoseconds) is expressed as the following convolution:
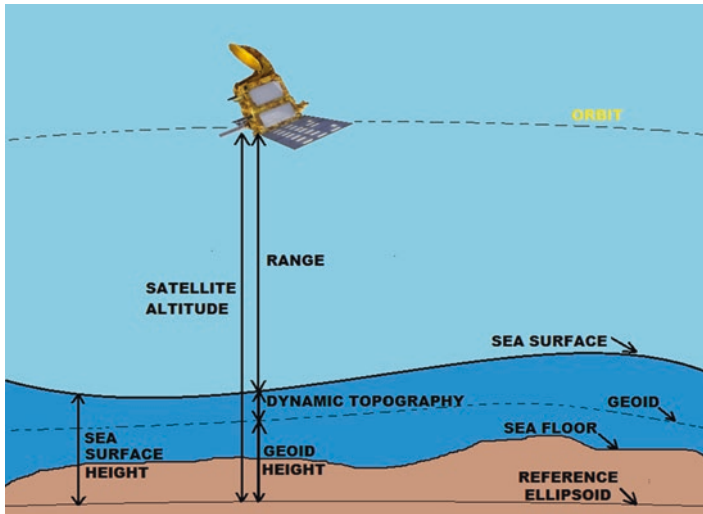
Fig. 3 Schematic representation of principles of satellite altimetry

$$W(t) = \text{FSSR}(t) * \text{PDF}(t) * \text{PTR}(t)$$

Calculation of the convolution with the assumption that mispointing angle is less than 0.3 degrees gives the analytical expression

$$W(t) = (A/2)\exp(-v)\big[1 + \text{erf}(u)\big]$$

where the auxiliary parameters u and v depend on the oceanic parameters of interest.

Geophysical parameters are obtained from altimeter data using retracking algorithms. In the open ocean, the waveforms are Brownian, and suitable algorithms exist for them [5]. Retrieval algorithm normally employed is physically based type and fitting algorithm is largely based on maximum likelihood estimator [58]. The algorithm retrieves mainly three parameters, namely the amplitude, the epoch (time passed since first return), and the backscatter coefficient. Least square method [47, 59] or Bayesian inference [61] are also employed to retrieve geophysical parameters. Accuracies of derived parameters from contemporary altimeters are ~0.3 m for SWH, ~3–4 cm for sea surface height anomaly (SSHA), and better than 2 m/s for wind speed. More complex waveforms normally encountered in coastal regions, continental waters, and over sea ice are retracked using empirical algorithms. Coastal altimetry, a new emerging domain under nadir-looking conventional altimetry, is described in detail in the next section.

3.4   Coastal Altimetry: A Challenging Task

In open ocean, satellite altimetry is a proven technology. Exploiting the high-rate altimeter data (20 Hz in the case of Jason-2 and 40 Hz for SARAL/Altika) for deriving coastal geophysical parameters is a challenging task. Coastal contamination in the footprint of the measurements requires dedicated classification, retracking strategy, and special treatment of atmospheric and geophysical corrections. In the coastal area, an altimetric waveform is corrupted because of the contamination caused by the presence of land in the footprint of the altimeter. For this reason, the waveforms measured in the coastal areas do not conform to the theoretical Brown model, and special data-processing efforts are needed for generating coastal waveform products. In fact, there are projects devoted specifically to the analysis of coastal waveforms, namely PISTACH [18] and COASTALT [30]. AltiKa was the first instrument to be operating at Ka-band (35-GHz) frequency with the bandwidth of 500 MHz that enabled a vertical resolution of 0.3 m instead of 0.5 m in Jason Ku-band [63]. A footprint of 3 dB in the case of AltiKa is 8 km as against 20 km in Jason altimeter. Along with this, high pulse repetition (4000 per second) results in better along-track sampling, enabling recovery of useful geophysical parameters near to the coast.

Normally, retracking algorithms appropriate for altimeter return echoes from open ocean that are based on the Brown model are not applicable for the coastal oceans. Hence, specific algorithms are to be devised for such echoes coming from coastal areas. Over the years, several retracking algorithms have been developed for specific surfaces, for example, Beta 5/9 algorithm [46] and the OCOG (offset center of gravity) technique [71]. These are also applicable for retracking of coastal waveforms. Guo et al. [32] proposed an improved threshold retracker, based on the leading edge detection and subwaveform extraction. Brown's model with the Gaussian peak model was developed by Halimi et al. [33] to model the contaminations caused by the land footprint in the form of Gaussian peak in the trailing edge of waveform. Launch of SARAL/AltiKa signifies a major leap in coastal altimetry owing to better signal-to-noise ratio, smaller footprint, and high along-track sampling. Altimeter footprint is the area of the surface over which the reflected power is accumulated over the designated number of gates for a single pulse. In the case of AltiKa, there are 128 gates, while for Jason-2 the number of gates are 104.

We will show a few examples to illustrate the usefulness of AltiKa instrument over Jason-2 for coastal applications. In Fig. 4a, SARAL/AltiKa ascending pass 223 (blue) and Jason-2 pass 155 (red) over the coast of Visakhapatnam (India) in the western Bay of Bengal are shown. AltiKa and Jason-2 waveforms as a function of distance from the coast near the Visakhapatnam region (east coast of India) are plotted over these tracks in Fig. 4b. Return power sampled in various gates (representing time elapsed since first return) is shown on y-axis. One can easily see that while waveforms in the case of Jason-2 get contaminated beyond 12 km shoreward, the same in the case of AltiKa show less contamination, and one can retrieve geophysical products up to 3–4 kms shoreward. SARAL/AltiKa waveforms in the open ocean and in the coastal region are shown in Fig. 4c. Another example of
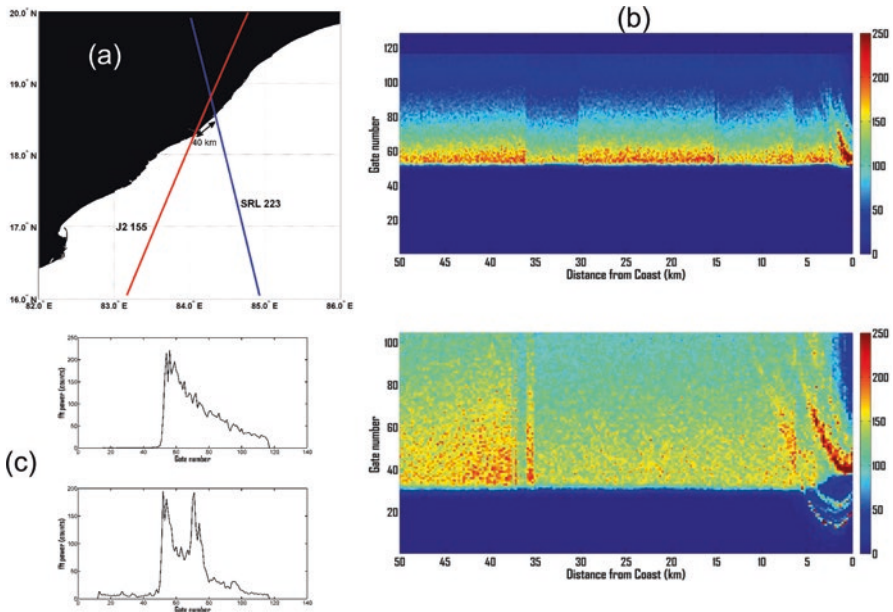
Fig. 4 (**a**) SARAL/AltiKa ascending pass 223 (*blue*) and Jason-2 pass 155 (*red*) passing along over the coast of Visakhapatnam (India) in the western Bay of Bengal (*upper*). (**b**) SARAL/AltiKa (*upper*) Ka-band waveforms and Jason-2 (*lower*) Ku-band waveforms are shown over these passes. X-axis denotes distance from the coast. (**c**) An example of typical waveform shape from open ocean (*upper*) and coastal region (*bottom*) from SARAL/AltiKa mission

cross-track surface current estimation from AltiKa and its comparison with currents measured by high-frequency (HF) radar is shown for the Chennai coast (east coast of India) in Fig. 5. One can see a good agreement of AltiKa current with HF radar currents.

3.5 Oceanographic Applications of Altimeter-Derived Parameters

Operational Oceanography is now well established, thanks to the efforts by various nations under Global Ocean Data Assimilation Experiment (GODAE) program, initiated in 1997, to understand the modeling and ocean forecasting needs. Altimetric measurements of sea level and significant wave height are the backbone of Operational Oceanography. The need to maintain the continuity of altimetric system for ocean forecasting is now firmly established. Altimeter-derived sea level and SWH are routinely assimilated in numerical models for generating ocean state forecasts. Forecasting the ocean state with 5–7 days lead time has several applications in the marine
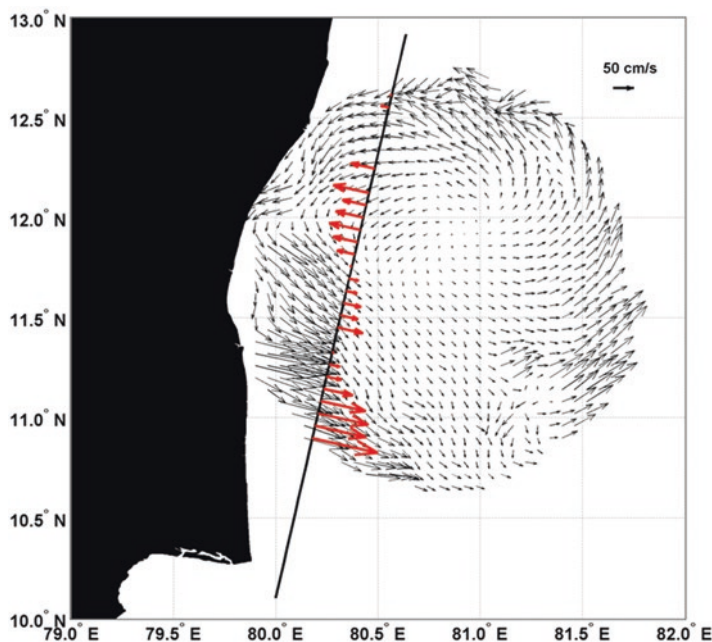
Fig. 5 A field of HF radar currents (in *black color*) near Chennai region on September 09, 2013. SARAL/AltiKa-derived across-track geostrophic currents (*red color*) computed for the track 868 for the same date are overplotted

fisheries, navigation, naval operations, oil-spill monitoring, etc. As the sea level, variations represent the integrated effect of the water column density variations; these data are now routinely used for hurricane forecasting [31]. Of course, this application requires merging of data from several altimeters. Altimeter-derived sea level anomaly are widely being used by researchers to monitor the progress of El Nino [38], as these events affect the climate and have impact on the economic conditions of nations. High-resolution altimeter data are being used to monitor inland river levels which may be useful for flood forecasting. Altimeter observations play a very important role in ice-sheet mass balance studies. Sea level rise is one of the most severe manifestations of the present-day global warming. Tide gauge and altimetric data from 1992 onward have revealed that global mean sea level (GMSL) has risen by 0.19 m between 1901 and 2010. The rate of increase in GMSL during 1993–2010 was 3.2 mm/year [64]. To capture this kind of small change, altimetric system needs to have a "mm" level control on the system drift. This calls for the continuity of mission, homogenization, and intercalibration of different altimeters to minimize the bias. Challenges associated with the accurate estimate of global sea level rise using satellite altimetry are provided in detail by Willis et al. [69].

3.6   GNSS-R and Swath Altimetry

Ocean Surface Topography Science Team (OSTST) and CEOS virtual constellation team consolidates the newer demands of global researchers, formulates the white paper, and coordinates the altimetric missions of various space agencies to maximize the benefits. Conventional altimeters which are nadir-looking measure the sea level only along the subsatellite tracks. Pascual et al. [52] have shown that four altimeters in a constellation resolve the mesoscale features in a more realistic manner. One way to enhance the coverage of nadir-looking altimeter is to have several altimeters in a constellation. A community white paper by Wilson et al. [70] highlights the requirement of multiple altimeters. Two new concepts, GNSS-R and Swath altimetry are described below.

Global Navigational Satellite System Reflectometry (GNSS-R) which works on the concept of bistatic radar is another emerging technology which can provide data on sea level, wind speed, and SWH on a large swath. Signals emitted by GNSS satellites (GPS, Galileo, and IRNSS) and reflected by ocean surface are received by low-orbiting satellites. GNSS signal consists of ranging codes known as C/A codes which belong to the family of pseudo-random noise (PRN) codes. GNSS signal is reflected from the earth, and the area which significantly contributes to the reflected signals is known as the glistening zone. These signals have a variety of delays (due to position) and Doppler frequency shifts (due to relative velocity). These shifts are mapped in receivers through a two-dimensional Delay Doppler Map (DDM). This DDM is then used to derive various parameters by using either theoretical models like that of the Zavorotny and Voronovich [73] scattering model or empirical relations [27]. This technology is still under demonstration phase.

The next available technology is the wide-swath altimeter [25], which will extend the observational capability of altimetry to the cross-track direction. It is expected that interferometric synthetic aperture radar processing of the returned signal, averaged over 1 square km, can give better than 2 cm height precision. The upcoming Surface Water Ocean Topography (SWOT) mission, proposed for launch in a few years is based on this technology. With ~130 km swath and an order-of-magnitude finer resolution, SWOT will represent a paradigm shift in the measurement capability. Along with oceanic mesoscale, submesoscale, and coastal observations, it would also contribute significantly to the land hydrology [26].

4   Satellite Scatteromerty: Measuring the Ocean Surface Winds

Ocean surface vector wind, being one of the major parameters of importance for forecasting of weather and ocean state, needs regular monitoring with good accuracy. A scatterometer is designed to measure ocean surface vector winds by utilizing the scattering mechanism of the incident microwave signal due to the surface waves [53]. The primary function of a scatterometer is to utilize backscatter dependence

on the radar azimuth to retrieve ocean surface wind vectors over the global oceans with 1–2 days interval. Surface winds are the major sources of momentum for the generation of surface waves and basin-scale ocean currents. Air-sea fluxes of heat, moisture, and gases are modulated by the action of winds. In this way, winds influence the regional as well as global climate. Thus, scatterometer, being an instrument to measure ocean surface winds in all weather conditions by using microwave signals, is one of the important space-borne sensors for the routine monitoring of the earth system processes.

4.1 Past, Present, and Future Scatterometers

Several scatterometers have been flown in the space by NASA, ESA, JAXA, and ISRO. Seasat launched by NASA in the year 1978 was the first operational scatterometer which operated at Ku-band (14 GHz) frequency and employed fan-beam system. Seasat provided global wind product at 50 km resolution on a swath of 750 km on each side. Subsequently, ESA launched ERS-1 Active Microwave Instrument – scatterometer at C-band (5.3 GHz), and NSCAT (Ku-band) was launched by NASA, once again with the fan-beam concept. Then came the generational shift in the scatterometry concept, when first pencil-beam scanning scatterometer "SeaWinds" onboard QuikSCAT was put in the orbit by NASA in June 1999. The operating frequency for this QuikSCAT was 13.6 GHz with large swath of 1800 km. QuikSCAT provided very useful wind product for nearly 10 years. Advanced SCATterometer (ASCAT) onboard Metop-A launched by EUMETSAT in 2006 operated at C-band. In the year 2009, ISRO launched OSCAT onboard Oceansat-2 satellite. It provided very useful data until March 2014. ISRO launched SCATSAT-1 in September 2016, which was a repeat mission of OSCAT with the same specifications. Also, there is a plan by ISRO to have scatterometer onboard Oceansat-3.

4.2 Basic Measurement Techniques: em Interaction with Roughness

A scatterometer is a side-looking radar system that transmits and receives microwave (electromagnetic) pulses. When the electromagnetic radiation transmitted from a scatterometer impinges on the ocean surface, most of the incident radiation gets scattered in different directions. Depending upon the roughness of the ocean surface, a portion of the incident radiation gets reflected towards the scatterometer antenna. This is called the phenomenon of backscattering. The backscattered power measured by the scatterometer is proportional to the surface roughness caused by

oceanic winds. If the winds with higher magnitude blow over the ocean surface, the surface roughness will be more and thus a scatterometer will receive more backscattered power and vice versa. However, such proportionality is not uniform throughout the possible wind speed regimes.

4.3   Retrieval of Ocean Surface Winds from Backscattering

The backscattered power intercepted by a scatterometer is measured in terms of backscattering coefficient or sigma-naught (σ^0). As mentioned earlier, the backscattered power and hence the σ^0 values are proportional to the wind speed, but the problem arises when researchers try to retrieve winds from σ^0. One can refer to the work by Ulaby et al. [65] for details on this aspect. However, for brevity, we briefly describe it here. Difficulty in retrieving winds emerges simply because scatterometer measures only the σ^0 that has the influence of the wind stress, but not the winds. Thus, the retrieval of the winds from the scatterometer measurements is basically an inverse problem where we need to find a suitable forward model for the σ^0 dependent on winds and then we need to invert that model to derive winds. It has been found that σ^0 is adequately described by the forward model:

$$\sigma^0 = a V^\gamma \left(1 + b \mathrm{Cos}\,\psi + c \mathrm{Cos}\,2\psi\right)$$

where a, b, c, and γ are constant for a given incidence angle, polarization and frequency, V is the wind speed, and ψ is the angle between the wind vector and the scatterometer look direction.

Such a forward model is known as geophysical model function (GMF) in scatterometer terminology. A GMF is developed by fitting collocated true winds (e.g., winds from in-situ observations like moored buoys, ships, etc.) and measured σ^0 values. In most of the cases, the GMFs are developed empirically, and they depend on the wind speed, direction, scatterometer incidence and azimuth angle (the direction along the track of the instrument) and polarization. Because of the wind direction dependence, a GMF exhibits biharmonic behavior over the various direction zones. In practice, the GMF is generally developed post-facto using collocated wind observations mostly from NWP model and the scatterometer observations over a period of several months covering the full dynamic range of wind vector. The GMF is essential for deriving the wind vector from scatterometer observations made by the same or similar scatterometer system. The GMF developed for one scatterometer system, in principle, can only be applied to the same system due to inherent characteristics embedded empirically in the derived GMF. However, its use with another system is possible provided the parameters of that system are kept unchanged or least deviated, which then can be further fine-tuned.

The exact behavior of radar backscatter varies with scatterometer operating frequency, polarization, radar azimuth and the incidence angle. It has been observed

over decades using earlier satellite missions and also based on theoretical models that radar backscatter depends upon wind speed with a power law while it depends biharmonically on wind direction. This harmonic nature of radar backscatter on wind direction leads to multiple possibility of wind vectors yielding the same radar backscatter value and thus causes ambiguity in wind direction determination. The radar backscatter decreases with incidence angle for a given wind speed and polarization. Moreover, radar backscatter from the ocean surface is more in vertical polarization than in the horizontal polarization.

The basic technique generally employed for extracting wind speed and direction from oceanic radar backscatter measurements made by space-borne microwave scatterometer makes use of the dominant dependence of radar backscatter on polarization and on wind speed and direction for a fixed observational geometry of scatterometer at the data location on ocean surface. The observational geometry varies across the swath for both types, viz. fan-beam and pencil-beam scatterometer systems. In the case of fan-beam scatterometer, the azimuth geometry remains unchanged with the incidence angle varying across the swath, while in case of pencil-beam scatterometer the incidence angle remains constant with azimuth angle varying across the swath. However, the constant parameters (depending upon the scatterometer type) change slightly due to the earth's curvature and the satellite orbit inclination and attitude. An example of scanning pencil-beam viewing geometry of SCATSAT-1 is shown in Fig. 6. SCATSAT-1 carries a scanning pencil-beam Ku-band scatterometer with a swath of 1800 km and wind vector cell size of 25 km × 25 km.

Assuming other parameters as constant and the dominant dependency of radar backscatter on ocean surface wind vector (speed and direction), extraction of wind speed and direction is carried out by comparing the measured radar backscatter with those simulated using suitable GMF for assumed wind speed and direction varied in its entire range valid for the GMF being used [28]. This process yields multiple solutions of wind vector among which one solution corresponds to true wind vector while others are ambiguities. The wind speed values of these vector solutions have small differences while the direction values are quite different. These solutions are prioritized according to the deviation of measured radar backscatter from the simulated values with the vector solution having minimum deviation treated as highest priority solution [29]. Under noise-free conditions, the highest priority vector solution always identifies the correct (true) wind vector, while under moderately noisy conditions, the highest priority solutions identify the correct wind vectors in about half of the data cases considered. Such performance of the algorithm is heavily dependent on the noise present in the radar backscatter data. The characteristic of these prioritized solutions is such that the majority of correct wind vector cases can be identified between the first two highest priority solutions. Moreover, in most of the cases, the directions of the first two highest priority solutions are mostly opposite to each other. Thus, when the wind vectors are retrieved from scatterometer data over the swath, about half of the directions may be found in opposite direction to the overall wind directional flow in the data region. These directional ambiguities are
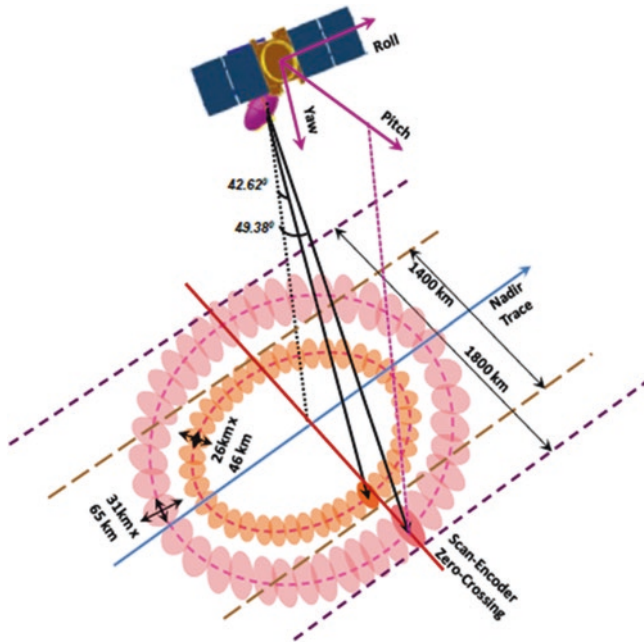
Fig. 6 SCATSAT viewing geometry (Source: SAC/SCATSAT/PDR/01)

filtered out by using another process known as directional ambiguity removal process.

4.4 Accuracy, Swath, and Resolution

The accuracies of the present-day scatterometer-derived winds are well within the research requirements. The mission requirements for a standard scatterometer-derived wind are less than 2 m/s RMSE in the wind speed and less than 20° in the wind direction. Once a scatterometer is launched, the data products that come from the scatterometer undergo rigorous calibration-validation (CAL-VAL) phase. For example, after the successful launch of Oceansat-2 Scatterometer (OSCAT), the initial 9 months of data from it was used for extensive CAL-VAL [10, 11]. The ocean surface winds derived from OSCAT were validated against observations from global moored buoys, winds available from NWP models, and other contemporary scatterometers [43]. Such extensive validation is required to establish the fulfillment of the mission-specific requirements [24].

The width of the sub-satellite track is defined as the satellite swath. The width of such swaths determines the coverage over the global surface. Depending upon the incident beam geometry, the swath varies for different scatterometers. For
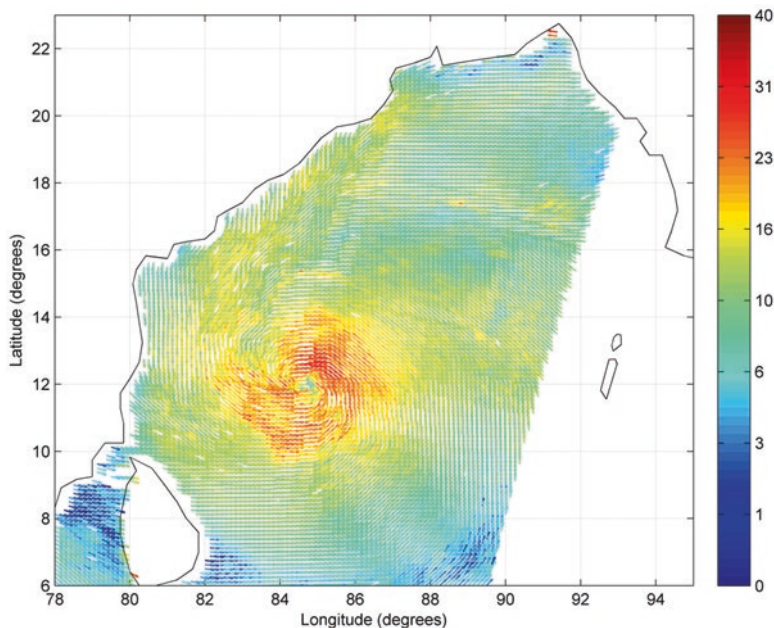
Fig. 7 OSCAT scatterometer derived wind fields on December 28, 2011 for the cyclone Thane

instance, QuikSCAT scatterometer launched by NASA in June 1999 had large swath of 1800 km for the outer beam which is quite similar for the case of OSCAT launched by ISRO in 2009. Large swaths of these scatterometers provided synoptic wind fields which helped in the studies of cyclogenesis and cyclone track prediction. Figure 7 shows one example of OSCAT-derived winds for the case of cyclone Thane. Advanced SCATterometer (ASCAT) onboard Metop-A launched by EUMETSAT in 2006 had two swaths each with 550 km separated by a nadir gap of 700 km.

The resolution of a scatterometer depends on various factors. The smallest element from which wind information from a scatterometer is obtained is called wind vector cell (WVC). The signals from multiple WVC are averaged to remove noises, and that leads to nominal resolution for operational product from a scatterometer. For example, the operational horizontal resolutions of the QuikSCAT, ASCAT, and OSCAT were 25 km, 25 km, and 50 km, respectively, though there were developmental finer resolution versions available.

4.5   Ocean and Ice Applications of Scatterometry

Ocean general circulation models (OGCMs) are forced by air-sea fluxes (wind stress, heat fluxes, and freshwater fluxes) at the ocean-atmosphere interface. Out of these surface boundary forcings, wind stress plays the leading role, particularly in the tropics, where the ocean circulation is primarily wind-driven. Hence, an accurate wind forcing is essential for simulating realistic circulation features [12, 13]. However, the surface wind vectors retrieved from a scatterometer are irregular in both space and time due to the limited beamwidth of the scatterometer geometry. Such scattered observations from scatterometers are analyzed to produce synoptic gridded wind vectors (analyzed wind vectors) regular in spatiotemporal coordinates [14] that are used to provide forcing to the ocean circulation as well as ocean wave models. Hence, the major application of scatterometer observation for oceanography is to provide forcing to the numerical ocean models. When it comes to applicability of scatterometer winds in ocean state forecasts, these winds are assimilated in the numerical weather prediction (NWP) models for providing the necessary forecasted surface boundary forcings for OGCM at more frequent time intervals (daily or even 6-hourly). Scatterometer-derived winds are also used to compute ocean surface currents along with altimeter observations. The phenomena of land and sea breeze along the coasts can also be studied using scatterometer data. Apart from this, scatterometer observations are utilized to monitor the extent and variability of sea ice. Here, the geophysical product that finds its application is the backscattering coefficient itself rather the ocean surface winds. Also, the scatterometer observations help in detecting large icebergs in the polar oceans.

4.6   New Concept in Scatterometry

The importance of scatterometer in met-ocean studies and operational forecasting purposes is now already established. There are several new upcoming concepts in scatterometer apart from the conventional configurations. A rotating fan-beam scatterometer named as RFSCAT will be flown in the Chinese-French Oceanic Satellite (CFOSAT). Also, engineering efforts are being engaged to develop scatterometer processor that will be doing the retrieval onboard. Efforts are also envisaged to measure the ocean surface currents along with ocean surface winds from a single scatterometer.

5   Synthetic Aperture Radar: Exploring Fine-Scale Processes

5.1   *Concept and Principles of SAR Technology*

Similar to the scatterometer systems, Synthetic Aperture Radar (SAR) is also an active radar, with a side-looking capability to observe various ocean, land, and atmosphere parameters, day and night, as well as practically in all weather conditions. In the lower frequency range of operations, they are also able to penetrate through clouds and light rains. General side-looking imaging radars work on the principle similar to the scatterometer with imaging capability, whereas Synthetic Aperture Radar provides the advantage of obtaining high-resolution images (~1 m) of the land and ocean surfaces. The basic difference between scatterometers, discussed in last section, and SAR is that SAR is able to provide high-resolution images of the targets, whereas scatterometers provide coarser resolution backscatter data.

The minimum area, which can be differentiated from the neighboring ones is called the resolution of the system. Basically, there are two types of resolutions, one in the direction of the spacecraft movement (azimuth resolution) and the other in the transverse direction (range resolution). Range resolution basically depends upon the width of the pulse. Radars achieve high resolution in range direction by transmitting a short pulse. Along-track or azimuth resolution of the radar is defined as βR, where β is the beamwidth of the antenna and R is the range of the target. The beamwidth is inversely proportional to the length of the antenna. In SAR system, the length of the aperture is synthesized to achieve high resolution.

Consider two objects A and B over the ground along the range direction (Fig. 8a). Assume that the satellite height is H, the range distance from the satellite to A and B are R_1 and R_2, respectively, the look angle is θ, and the pulse separation time is τ. If A$^{'}$ is the projection of object A along the slant range, to resolve the two objects along the slant range direction, the minimum distance traveled by the incident pulses should be (R_2-R_1), that is, the slant range resolution should match the criterion given by

$$2R_2 / C - 2R_1 / C >= \tau, \text{where } C \text{ is speed of light}$$
$$\text{or,} \left(R_2 - R_1 \right) >= C^* \tau / 2$$

Along the ground range, the projection of (R_2-R_1) will be (R_2-R_1)*sin θ. Hence, the ground range resolution of a SAR system will be

$$\left(R_2 - R_1 \right) >= C^* \tau / \left(2^* \sin\theta \right)$$

Next, we consider azimuth (along-track) resolution (Fig. 8b). We focus on a smallest element over the satellite swath. Suppose a signal is emitted from the radar and it reflects back from different targets. The signal from the point opposite the antenna reaches first the center of the antenna and later the ends of the antenna, that
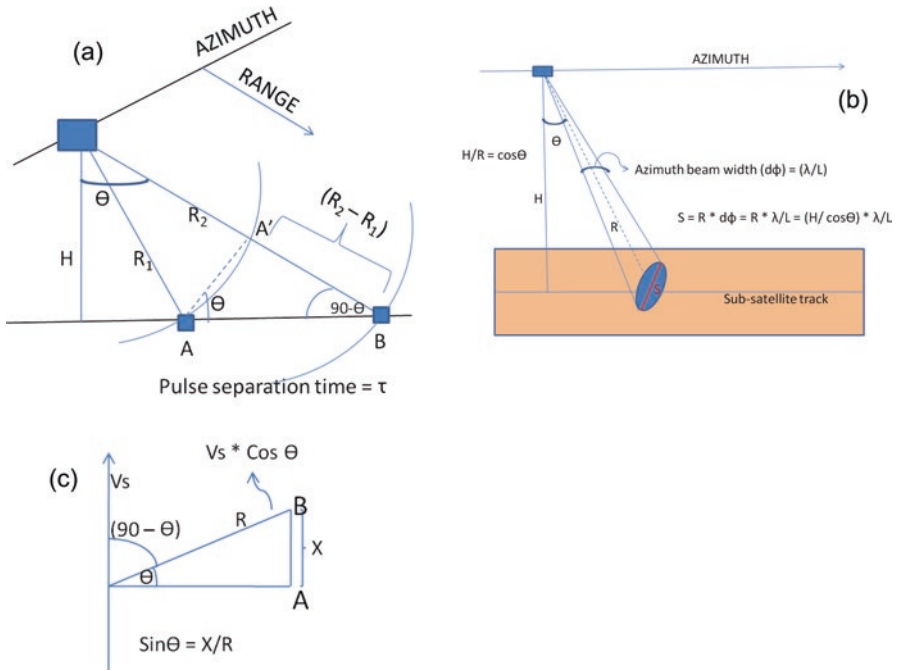
Fig. 8 Synthetic aperture radar (**a**) range (across-track), (**b**) azimuth (along-track) resolution measurement principles, (**c**) concept of Doppler shift

is, small phase change will occur along the aperture, but phase distribution will be symmetrical about the center, and the overall summation of signal across the aperture will be constructive. But, if the target is toward one end of antenna, the phase change around the center of antenna will not be symmetric, and hence destructive interference will occur, and when the signal is integrated, it will not contribute to the signal. Similar things will happen for targets between these two points. The larger the aperture of antenna, the closer the point from the center will try to create destructive interference and will not contribute to received signal; hence, resolution will be higher. SAR uses the same principle, but instead of using larger antenna, it uses smaller antenna, and signal is integrated over a long period of time.

If R is the range distance to the central point of the element and θ is the look angle, then from geometry we get H/R = cos θ. The azimuth beam width β is defined as

$\beta = \lambda/L$, where λ is the radar wavelength and L is the antenna length. Thus, the radar azimuth resolution (S) can be computed as

$$S = \beta R = \lambda / L \cdot R = \left(H / \cos\theta \right)^* \lambda / L.$$

At this stage, let us consider an interesting example. The following are the provided specifications of RISAT-1 SAR:

$\lambda = 5.6$ cm $= 0.056$ m (f $= 5.35$ GHz)
$H = 580$ km $= 580{,}000$ m
$L = 6$ m
$\theta = 25^0$ (say)

For this configuration, the azimuth resolution can be computed as

$$S = (0.056 * 580000)/(6 * \cos(25)) = 5972\,\text{m}$$
$$= 5.9\,\text{km which is too large for a sensor like SAR.}$$

RISAT-1 SAR is having various mode-specific resolutions, ranging from 2 to 50 m. For instance, if $S = 10$ m, then the required antenna length can be computed as

$$L = \lambda * H/(Ys * \cos\theta) = 0.056 * 580000/(10 * \cos(25)) \approx 35\,\text{km}$$

It is practically impossible to mount such a big antenna onboard a SAR system. To mitigate this problem, SAR continues to look at a particular object for a sufficient dwell time, and during that time the distance traveled by the sensor is used as a synthetic aperture length to process the SAR signal, and thus the fine resolution is achieved along the azimuth.

Now, consider SAR system is moving with the speed Vs and along the azimuth there are two nearby objects A and B separated by a distance X (very small in magnitude). If R is the range distance and θ is the look angle, then from geometry (Fig. 8c) we get

$\sin\theta = X / R$. Now if we recall basic Physics, we can define Doppler frequency as

$f_o = (1 + v/c)\, f_s$, where the subscript "o" and "s" stand for observer and source frequency, respectively, v is the relative speed between them, and c is the speed of light. So, the Doppler shift is

$$df = f_o - f_s = (v/c)f_s = v/\lambda, \quad \lambda\left(= f_s/c, \text{being the wavelength of the source signal}\right).$$

Hence, the total Doppler shift (approaching + receding) = $\Delta f = 2 * df = 2* v/\lambda$. For side-looking SAR, $v = Vs * \cos(90 - \theta) = Vs * X/R$
So, $\Delta f = 2 * Vs * X/(\lambda * R)$
Now, for a small shift, $\delta(\Delta f) = \{ 2*Vs/(\lambda * R) \} * \delta X$.
SAR integration time, Tint $= 1/\delta(\Delta f) =$ Footprint/sensor velocity $= (\lambda/L) * R/Vs$.
On using the above two expressions, we get $\delta X = L/2$.

Thus, the azimuth resolution of SAR is just half the antenna length. However, to achieve much finer resolution, the antenna length cannot be simply reduced because the sampling bandwidth (or the pulse repetition frequency or PRF) must be greater or equal to Doppler bandwidth, that is,

$$\text{PRF} >= Vs\,/\,\delta X \text{ which implies } \text{PRF} >= 2Vs\,/\,L.$$

These computations are well valid for the land-based targets where Doppler shift happens because of the relative velocity between the fixed targets and the SAR sensor. In case of moving targets, for example, ocean surfaces, there will be an additional velocity component from the motion of the targets.

For such a situation, SAR data processing becomes more complicated.

5.2   Ocean Surface Imaging

The high resolution by SAR relies on the precise measurement of phase and Doppler and signal processing. The SAR signal processing has the assumption that the Doppler shift of the signal is due to the movement of SAR system, whereas the inherent motion of the object in consideration also produces a Doppler shift and affects its appearances in SAR image. The backscattered signal received by a SAR receiver is due to the interaction of the transmitted signal whose characteristics are determined by the radar's frequency, polarization, viewing geometry, and the target surface whose characteristics depend on roughness features, electrical properties, and material composition. Over the ocean surface, SAR energy is primarily scattered by the presence of small-scale wind-induced capillary waves. For the ocean imaging, the surface is always in motion, and the mean wave structure will include a variety of motions with components along the line-of-sight to the radar. These motions will induce Doppler frequency shifts on the backscattered signal. These shifts, and the resulting misregistration of scene scatterers, produce a smearing or blurring in the azimuth direction. These shifts tend to be different for different phases of the dominant (long) waves, and the magnitude of the effect depends primarily on significant wave height and other parameters. This phenomenon is called velocity bunching. It is a limiting factor in a SAR's ability to image ocean wave fields

Similar effect is also observed from other moving objects such as ships, which are displaced from their actual position, and trains that appear to be moved from the railway tracks. The ocean features commonly seen on SAR imagery include surface waves, mesoscale ocean circulation features such as eddies and currents, oil slicks, and surface manifestations of internal waves, and subsurface currents over shallow shoals. In addition to the wind speed, one can also get information on the patterns and structures of winds within the atmospheric boundary layer.

The interactions of short and long waves affect the radar scattering by a process known as the two-scale scattering theory. There are three primary mechanisms in which long waves modify the Bragg waves to effect SAR imaging: the hydrodynamic, tilt, and velocity bunching [1, 2, 4, 21, 34]. The hydrodynamic modulation occurs due to the modulation of the energy of short ripples through interaction between ripples and long waves. The small-scale waves ride upon the large-scale waves somewhat nonuniformly. Due to the different directions of the orbital velocities of long waves along the wave, short waves pile up at the crest and spread them out in trough. Tilt modulation is purely due to the geometric effect that Bragg scattering waves are seen by radar at different local incidence angles depending upon the slope of long-scale waves. This effect is independent of hydrodynamic interaction and will occur even if ripples are uniformly distributed over the longer waves.

In the case of actual ocean surface, as long waves grow steeper, the radial velocity components increase, resulting in more random azimuth displacements and smearing in the imagery. This effect reduces the azimuth resolution and thus limits the detectable ocean wavelengths. The azimuth shift is estimated by the distance between the radar and the surface and its velocity.

5.3   Retrieval of Oceanographic Parameters

High-resolution surface images from SAR over the oceans contain signatures of the surface features. Hence, it is possible to retrieve information about those features by interpreting or processing the SAR images. One of the important applications of SAR is the retrieval of ocean surface wave information. In general, a wave field consists of a number of waves with different wavelengths and directions. The best way to extract wave information from SAR image is by analyzing the power spectrum. All dominant wave peaks can be seen in the power spectrum, which is obtained by taking the square of 2D Fourier transform of image data. However, due to system response and noise, different corrections have to be applied to obtain noise-free image spectrum, but not ocean wave spectrum.

The ocean wave spectrum S(K) results after applying modulation transfer function, consisting of tilt, hydrodynamic modulation and velocity bunching, to the SAR image spectrum. The linear and nonlinear schemes, depending upon the ocean conditions, have been generally used for the inversion of SAR image spectra to ocean wave spectra [21, 38].

The wave height can be estimated by

$$\mathrm{SWH} = 4.0 \times \mathrm{Energy}$$

where $\mathrm{Energy} = \int S(K) \, dK$
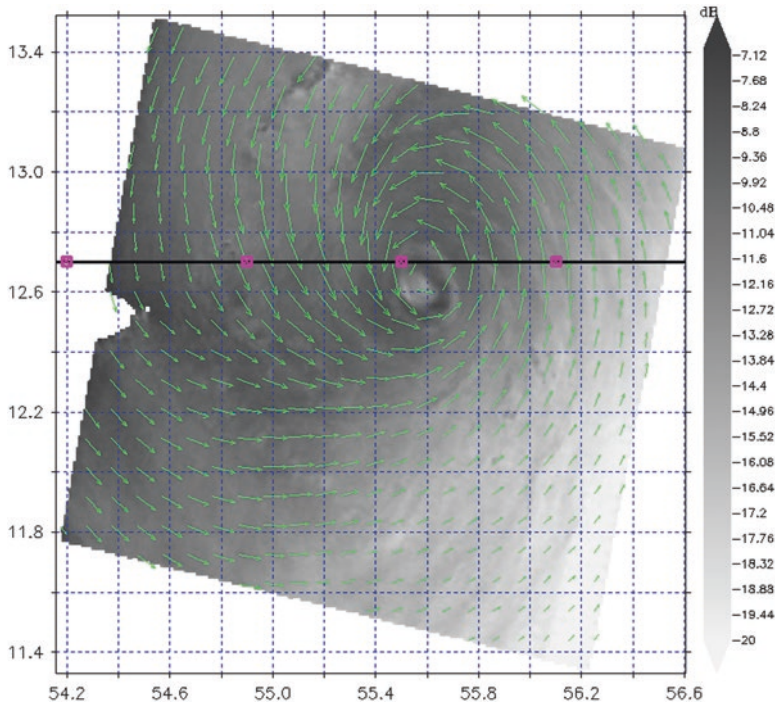
Fig. 9 RISAT-1 SAR image (VV-Pol) of cyclone Megh acquired on November 08, 2015. Wind direction derived from the SAR image (*green arrows*) overlaid on the SAR image. Cyclone track data (November 7–8, 2015) are from Joint Typhoon Warning Centre, shown by the *black line*

SAR is able to retrieve high-resolution and wide-coverage wind fields for applications where knowledge of the wind field is crucial. With the SAR-derived wind fields, one is now able to position atmospheric fronts and lows to a high accuracy. The high-resolution wind fields help in many applications like weather prediction, cyclone studies (Fig. 9), climate research, risk management, and commercial applications like energy production, ship routing, and structure design to operate in coastal environment. SAR-derived wind fields are also useful in wave retrieval by providing a first guess wind wave spectrum.

There are different types of techniques for wind retrieval. One of them is scatterometry-based approach. This is based on the idea that as the wind blows across the surface, it creates surface roughness commonly aligned with the wind. Consequently, the radar backscatter arising from this roughened surface is related to the wind speed and direction [37]. The dominant mechanism for scatterometer and SAR incident angles is Bragg's scattering, which means that the dominant return is proportional to the roughness of the ocean surface on the scale of the radar wavelength.

To retrieve winds from SAR imagery, image calibration is required to convert the digital number values of the imagery into the backscattered power. Calibration

process requires the information of the external calibration constant and the local incidence angles. The calibrated SAR image is then inverted to obtain the wind speed using a Geophysical Model Function (GMF) and using auxiliary information of wind direction from NWP models or based on the information embedded in the data itself seen as wind streaks. Most of the GMF developed presently are based on VV polarization SAR images. However, the wind retrievals from HH polarized images are performed using an azimuth and incident angle-dependent parameterization for the effective polarization ratio [50]. SAR is also capable of estimating high-magnitude cyclonic winds with good accuracy [36].

5.4   Oceanographic Applications of SAR

SAR provides a two-dimensional image of the sea surface. Surface waves can be clearly seen in SAR images. Since the surface waves are formed primarily in response to surface winds, winds can be derived by SAR. Detection of upper layer circulation features including fronts, eddies, upwelling, internal waves, tidal circulation, bottom topography, and ship speeds have been demonstrated using SAR data. Due to lack of space-borne data between SEASAT in 1978 and ERS-1 in 1991, the studies were somewhat limited. Most of the studies have been obtained through airborne system; however, since the launch of ERS-1, SAR data has been regularly available and a large number of demonstrative studies have been conducted.

Ocean surface currents can also be retrieved from SAR imagery. However, this requires along-track interferometric configuration of the SAR antenna. This configuration has two antennas. One transmits and receives in usual way while the other antenna is used for only receiving. Interferometric configuration is not common for all the available SAR sensors. From the SAR systems without interferometric capability surface currents can be measured but only along the range direction (single component only) by using Doppler shifts. However, one-component currents thus retrieved have limited usability.

Monitoring of coastal bathymetry is vital for the exploitation of living and non-living resources, operations on engineering structures, and ocean circulation studies. The estimation of shallow water bathymetry depends upon the refraction of deepwater wavelength and wave direction in the shallow region. With the propagation of long waves toward the shallow region, waves start feeling bottom, and their wavelength as well as direction changes [43, 60]. Another method of deriving bathymetry is more complex, however it provides better estimates. In this approach, imaging mechanisms, consisting of various interaction processes, such as depth-current interaction, current-wave interaction, and wave-radar interaction, are being used. To estimate the bathymetry, the interaction mechanisms discussed above are inverted using a data-assimilation approach in conjunction with SAR data and a limited amount of in-situ data. [3, 9, 67].

It might be surprising that SAR, being a surface-viewing sensor, is also able to detect processes which take place within the sea and particularly at the thermocline.

Internal waves are waves that travel underneath the ocean surface. They are generated and propagated along the interface between waters of different densities. Due to large amplitude and orbital velocities, manifestations of these waves can be seen on the surface. The signature on the surface of ocean due to internal waves is related to the convergence of surface velocities at the surface above the slope behind the wave crest. Characteristics of the internal waves from a SAR image can be estimated using Fast Fourier Transform Technique (FFT). Pollution of the sea surface by mineral or petroleum oil is a major environmental problem. Despite the International Convention for Prevention of Pollution from ships, large quantities of mineral oil are still being discharged from ships in these special areas. SAR images are also very useful in the detection of oil spills.

The strong signals from targets like ships make SAR systems particularly useful for detecting vessels at sea. Ships are detected by three mechanisms: by observing radar backscatter directly from the ships; by detecting the wake of ships, and by identifying surface slicks resulting from ship engines. Other phenomena revealed by SAR include the detection of current patterns, eddies, and gyres, by their influence on surface waves. In addition to ocean features, SAR imagery is also being used to detect and identify various features such as ice type, ice edge, icebergs, and ice islands. SAR-derived wave spectra have the capability of assimilation in wave prediction models; however, operational use of such spectra or wind is limited by the lower repetivity and smaller coverage over the oceans. The Advanced SAR (ASAR) onboard EnviSAT as well as Sentinel-1 has an additional wave-mode acquisition dedicated for the retrieval of waves and winds only.

5.5   Future Advancements in SAR

For the last four decades, high-resolution imageries over the ocean surfaces captured by various tandem SAR missions have been providing resourceful information to the research community. At present scenario SAR is capable of working in monostatic mode, which suffers from receiving a major portion of the backscattered signals. To avoid this, the idea of bistatic SAR has already been conceptualized. Efforts are being dedicated presently over the globe to implement such systems practically. Also, several SAR constellations are being planned. ISRO has planned a follow-on mission of RISAT-1 as RISAT-1A. NASA and ISRO have also planned a joint dual frequency (L-band and S-band) SAR mission, to be launched in 2021, known as NISAR.

6   Remote Sensing of Ocean Salinity: Filling the Missing Gap in Ocean Observation

Sea surface salinity (SSS) variations are key indicators of the hydrological cycle encompassing evaporation, precipitation, freezing/melting of ice, and river run-off. There have been several studies that highlight the importance of SSS for ocean circulation and climate change. A special section on ocean salinity in the *Journal of Geophysical Research* [45] highlights the importance of this parameter in a wide variety of ocean studies.

Ocean salinity can be measured accurately with ships, buoys, and Argo floats at different depths in the ocean, but such measurements are very sparse. Although with the availability of the Argo floats, the salinity observations have considerably increased, still satellite-based observations with better spatial and temporal coverage hold a very good promise. Ocean average surface salinity is about 35 psu with a range of 32–37 psu, however the regions which are strongly affected by river water, salinity can go down to as low as 26–27 psu. Salinity retrieval from space is relatively a new concept. Soil Moisture and Ocean Salinity (SMOS) and Aquarius were the dedicated space-borne salinity missions that paved the way for a new era in ocean remote sensing.

6.1   Satellite Instruments for Salinity

The satellite, Soil Moisture and Ocean Salinity (SMOS), for the estimation of ocean surface salinity was launched in November 2009 by ESA. SMOS makes observations at 1.4 GHz using Microwave Imaging Radiometer with Aperture Synthesis (MIRAS) instrument for the surface salinity observation over ocean and surface soil moisture over land. SMOS used a dual-polarized L-band radiometer and adopted the 2D aperture synthesis technique to achieve a ground resolution better than 50 km without putting a large antenna into the orbit [40]. Subsequently, NASA launched Aquarius mission in June 2011 that carried three radiometers and a scatterometer having swath of 390 km. Aquarius provided salinity using 1.4 GHz passive microwave measurements with an accuracy of 0.2 psu on a monthly scale. Measurement of the ocean surface salinity from Aquarius was based on a real aperture 3-beam push-broom design. Aquarius was a dedicated surface salinity mission with enhanced capability in terms of better signal-to-noise ratio. Unfortunately, it suffered from failure in the power supply, and the mission ended in June 2015. The Soil Moisture Active and Passive (SMAP) mission by NASA (in collaboration with JAXA) was launched in January 2015. Although the primary objective of SMAP was the estimation of soil moisture over land, its 1.4 GHz passive radiometer had

the potential for the estimation of ocean surface salinity. The SMAP [7, 22] mission, with both active and passive instruments, provides SSS at a spatial resolution of 40 km over a wide swath of ~1000 km, which is a clear advantage over coarser resolution (100–150 km) and narrower swath (390 km) from Aquarius. The L-band synthetic aperture radar (active sensor) onboard SMAP stopped functioning during July 2015, but salinity data continues to be derived from this instrument.

6.2 Measurement Principles and Challenges for Salinity Retrieval from Space

Theoretical basis for ocean salinity retrieval from passive microwave radiometric measurements is to exploit the sensitivity of emission to ocean salinity through its effect on dielectric constant of water. Dielectric constant of water decreases with the increase in salt content. Figure 1 shows the relative sensitivity of microwave radiometer frequencies for various oceanic parameters which shows that the sensitivity of microwave brightness temperature for sea surface salinity is maximum towards the lower frequency. 1.4 GHz is considered the best frequency for salinity retrieval as below this frequency there is significant radio frequency interference due to man-made RF transmitters. This frequency is least sensitive to SST, surface roughness, atmospheric water vapor, and liquid water content. Hence, salinity can be retrieved primarily from passive radiometer at L-band microwave frequency, with scatterometer or synthetic aperture radars used for correcting the surface roughness effect. For salinity retrieval, normally mono-frequency is preferred. The salinity retrieval algorithm is normally based on an iterative convergence approach which minimizes the difference between the satellite radiometer-measured brightness temperature and those generated from forward radiative transfer model. Forward modeling is performed for ocean surface emissivity which depends on the sea state, SST, viewing angle, and polarization. RT model also includes the atmospheric effects, galactic radiation contamination, and the sun-glint effect.

One of the very important points in salinity retrieval is that although the sensitivity is very small one has to take into account the effect due to sea surface roughness, SST, foam, sun-glint, rainfall, ionospheric effects, and galactic background impact on the brightness temperature. Another very important point to be remembered is the low sensitivity of brightness temperature to salinity (0.75 K at 30 °C, 0.5 K at 20 °C, and 0.25 K at 0 °C) that puts a stringent requirement on the radiometer to have a very high signal-to-noise ratio. Additional requirements are multiangular and multipolarization measurements. Low sensitivity of brightness temperature to salinity requires more energy to be gathered so that it is above the noise level, and hence footprint of the radiometer needs to be large. The active sensor scatterometer, onboard Aquarius, and the synthetic aperture radar, onboard SMAP, were used for

correcting surface roughness effect on the brightness temperature. As mentioned earlier, SAR sensor onboard SMAP has stopped working. SMAP instrument [7] employs a single horn, with dual-polarization and dual-frequency capability (radiometer at 1.41 GHz and radar at 1.26 GHz). The SMAP radiometer provides a real aperture resolution in which the dimensions of the 3 dB antenna footprint projected on the surface meets the 40-km spatial resolution requirement. The radiometer measures four Stokes parameters at 1.41 GHz to provide a capability to correct for possible Faraday rotation caused by the ionosphere. The chosen 6-AM/6-PM sun-synchronous orbit configuration also minimizes such Faraday rotation.

6.3   Accuracy and Spatiotemporal Sampling

Global observation of ocean salinity with an accuracy of 0.1 psu, every 10 days at 200 km spatial resolution, was envisaged under GODAE. The passive microwave radiometers have a major limitation in resolving small-scale salinity gradients due to their coarser spatial resolution (~40–100 km). The SMOS instrument uses a synthetic aperture antenna that yields multiangular brightness temperature mapping at about 40-km resolution. The Aquarius mission had a revisit of 7 days and provided global maps of SSS with accuracy of 0.2 psu at 150 km resolution on a monthly timescale. The SMAP has a higher spatial resolution of 40 km and a wider swath of 1000 km that enable global coverage in 2–3 days. The finer spatial resolution of the SMAP makes it noisier than Aquarius, but the noise is reduced by larger temporal averaging. Therefore, SMAP provides only 8-day running mean and monthly SSS product.

In the Indian Ocean, Ratheesh et al. [56] validated Aquarius SSS with the Argo data for the period 2011–2012. The coefficient of determination between SSS and reference measurements was found to be 0.84, and root mean square difference (RMSD) was about 0.45 psu. A similar analysis was performed by Ratheesh et al. [55] with daily level 3 product of SMOS SSS on a grid of 0.25 × 0.25 deg. Limited validation showed SMOS SSS accuracy of 0.36 psu and 0.34 psu at two RAMA buoys in the Indian Ocean. Drucker and Riser [17] found that Aquarius level 2 salinity differs from Argo salinity by +0.018+/−0.42 psu on a global scale.

Aquarius was declared nonfunctional in May 2015, leaving, once again, a huge void in salinity measurements over the global oceans. Since April 2015, SSS data from NASA's Soil Moisture Active Passive sensor is made available at http://www.remss.com/missions/smap [49]. Figure 10 shows a plot of sea surface salinity from SMAP averaged for August 21–September 18, 2015 in the Bay of Bengal. During this time, in-situ salinity measurements from the thermosalinograph were available from the US R/V Roger Revelle under the joint ASIRI-OMM program [68]. These observations along the ship track are overlaid on SMAP salinity (Fig. 10). Figure 10 indicates that the quality of salinity from SMAP is promising.
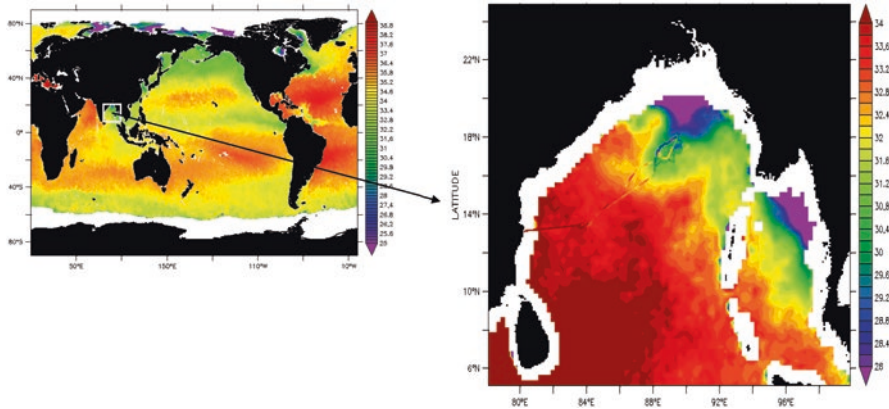
Fig. 10 Averaged (August 21–September 15, 2015) sea surface salinity (psu) from Soil Moisture Active and Passive Sensor. Surface salinity data from thermosalinograph of R/V RogerRevelle cruise in the Bay of Bengal for the same period are overlaid on SMAP salinity (blown-up image) (TSG data courtesy: Prof Jonathan D. Nash, Oregon State University. SMAP data source: Beta version release by Remote Sensing Systems – https://remss.com)

6.4 Applications of Satellite-Derived Salinity

Ocean surface salinity is increasingly being recognized as a key parameter in ocean-atmosphere interaction. Apart from taking part in this interaction, surface salinity plays a vital role in oceanography in the stand-alone mode also by influencing ocean dynamics and thermodynamics [20]. In the tropical Pacific, an in-depth understanding of the dominant El Nino Southern Oscillation (ENSO) event using numerical ocean circulation models is just not possible without a faithful representation of SSS in these models [39, 48, 51]. Knowledge of the global salt distribution and its variations is critical to understanding the role of oceans in the climate system. It is well established that ocean circulation, air-sea heat exchanges, and heat transport play important roles in regulating the climate. Three-dimensional ocean flow which is famously known as "thermohaline circulation" is largely governed by salinity variations due to evaporation and ice melting/freezing. Ocean surface salinity is linked to evaporation minus precipitation. Hence, measuring salinity will be helpful to constrain the estimation of E-P and will help in better estimate of air-sea flux. Using 50 years' of observed global surface salinity changes and climate model simulations, there is evidence of intensified global water cycle at a rate of 8 +/− 5% per degree of surface temperature warming [19].

The hydrological cycles in the ocean and atmosphere are intimately linked. This linkage is even much stronger in the river-dominated Bay of Bengal due to heavy river discharge. The stability caused by freshening isolates the upper layer of north-

ern Bay of Bengal from its interior, which results in a strong barrier layer. Observations suggest that storm-induced vertical mixing is limited to the upper warm layer which favors intense tropical cyclones in this region. Salinity from space will help unravel many unanswered processes at play in such regions.

Another very important aspect of global salinity measurements from space is its assimilation in models to improve the ocean state estimation for ocean process studies. Model simulations in the tropical Indian Ocean show surface salinity variability in the range from 0.2 to 1.5 psu, with larger values in regions with strong seasonal transitions of surface currents (south of India) and along the coast in the Bay of Bengal [62]. Assimilation of surface salinity from Aquarius (NASA Salinity Mission) and surface temperature from AVHRR [12, 13]) has shown positive impact on Indian Ocean equatorial jet simulation.

7   End Remarks

This chapter summarized the development of satellite oceanography over the years. It is now well established that satellite observations are integral components of ocean research and applications. Immense work has been carried out using the data from various satellites working in different regions of the *em* spectrum. Still there are several challenges in terms of sensor resolution, retrieval accuracy, and continuity of the missions. Exploiting the full potential of altimetry in the coastal region is an active area of research. Making use of opportunity signals from global navigational systems for extracting useful ocean information is another emerging field. Nadir altimeters are in operation for so many years now, new concept of swath altimetry (SWOT mission) will revolutionize the science of altimetry. Improvement in spatial resolution with microwave instruments requires advanced signal processing. With a lot of data coming now from in situ platforms, one needs to understand how best one can synergistically combine the in-situ and satellite data to address many unresolved problems of ocean research. There is also a need to adopt sophisticated data-mining approach to handle vast amount of ocean data obtained from satellite platforms. Another important aspect is to have coherent and coordinated efforts by different space agencies to plan out satellite constellation and maintain the continuity of the missions. In this regard, multimission science teams and virtual constellation teams under the umbrella of Committee on Earth Observation Satellites (CEOS) are working together to define data policy and evolve user requirements.

References

1. Alpers W (1983a) Imaging ocean surface waves by synthetic aperture radar: a review. Satellite Microwave Remote Sensing. Hg. Allan, T. D, England: Ellis Horwood, Chapter 6, pp 107–119
2. Alpers W (1983b) Monte Carlo simulations for studying the relationship between ocean wave and synthetic aperture radar image spectra. J Geophys Res Oceans 88(C3):1745–1759
3. Alpers W, Hennings I (1984) A theory of the imaging mechanism of underwater bottom topography. J Geophys Res 89:1029–10546
4. Alpers W, Ross DB, Rufenach CL (1981) On detectability of ocean surface waves by real and synthetic aperture radar. J Geophys Res 86:6481–6498
5. Amarouche L, Thibaut P, Zanife O-Z, Dumont P, Vincent J-P, Steunou N (2004) Improving the Jason-1 ground retracking to better account for attitude effects. Mar Geod 27:171–197
6. Bhowmick SA, Kumar R, Kiran Kumar AS (2014) Cross calibration of the OceanSAT-2 scatterometer with QuikSCAT scatterometer using natural terrestrial targets. IEEE TGRS 52(6). https://doi.org/10.1109/TGRS.2013.2272738
7. Brown ME, Escobar V, Moran S, Entekhabi D, O'Neill PE, Njoku EG, Doorn B, Jared K (2013) NASA's Soil Moisture Active Passive (SMAP) mission and opportunities for applications users. Bull American Met Soc 94(8):1125–1128
8. Brown GS (1977) The average impulse response of a rough surface and its applications. IEEE Trans Antennas Propag AP-25:67–74
9. Calkoen CJ et al. (1993) The imaging of sea bottom topography with polarimetric P-, L-, and C-band SAR. Report BCRS project 2.
10. Chakraborty A, Deb SK, Sikhakolli R, Gohil BS, Kumar R (2013a) Intercomparison of OSCAT winds with numerical model generated winds. IEEE Geosci Remote Sens Letts 10:260–262
11. Chakraborty A, Kumar R, Stoffelen A (2013b) Validation of ocean surface winds from the OCEANSAT-2 scatterometer using triple collocation. Rem Sens Letts 4(1):85–94
12. Chakraborty A, Sharma R, Kumar R, Basu S (2014a) A SEEK filter assimilation of sea surface salinity from Aquarius in an OGCM: Implication for surface dynamics and thermohaline structure. J Geophys Res (Oceans) 119:4777–4796
13. Chakraborty A, Sharma R, Kumar R, Basu S (2014b) An OGCM assessment of blended OSCAT winds. J Geophys Res (Oceans) 119:173–186
14. Chakraborty A, Kumar R (2013) Generation and validation of analysed wind vectors over the global oceans. Remote Sens Lett 4(2):114–122
15. Chelton DB, Ries JC, Haines BJ, Fu L-L, Callahan PS (2001) Satellite altimetry. In: Fu L-L, Cazenave A (eds) Satellite altimetry and Earth sciences: a handbook of techniques and applications. Academic, San Diego, pp 1–132
16. Donlon CJ et al (2007) The GODAE high resolution sea surface temperature pilot project (GHRSST-PP). Bull Am Meteorol Soc 88:1197–1213
17. Drucker R, Riser S (2014) Validation of Aquarius sea surface salinity with Argo: analysis of error due to depth of measurement and vertical salinity stratification. J Geophys Res (Oceans) 119:4626–4637
18. Dufau C, Mercier F, Bouffard J, Bronner E, Lombard A, Picot N, CLS PISTACH Team (2009) Improved Jason-2 altimetry products for coastal ocean: PISTACH. Geophysical Research Abstracts, vol 11, EGU2009-8980, EGU General Assembly

19. Durack PJ, Wijffels SE, Mater RJ (2012) Ocean salinities reveal strong global water cycle intensification during 1950 to 2000. Science 336:455–458

20. Durand F, Gourdeau L, Delcroix T (2003) Can we improve the representation of modeled ocean mixed layer by assimilating surface-only satellite data? A case study for the tropical Pacific during the 1997–1998 El Nino? J Geophys Res 108(C6):3200. https://doi.org/10.1029/2002JC001603

21. Elachi C, Brown WE (1977) Models of radar imaging of the ocean surface waves. IEEE Trans Antennas Propag AP-25:84–95

22. Entekhabi D et al (2010) The Soil Moisture Active Passive (SMAP) Mission. Proc of the IEEE 98.5 (2010):704–716 Copyright 2010 IEEE.

23. Flament P, Firing J, Sawyer M, Trefois C (1994) Amplitude and horizontal structure of a large sea surface warming event during the Coastal Ocean Dynamics Experiment. J Phys Oceanogr 24:124–139

24. Freilich MH, Dunbar RS (1999) The accuracy of the NSCAT-1 vector winds: comparisons with National Data Buoy Center buoys. J Geophys Res 104(C5):11231–11246

25. Fu L-L, Alsdorf D, Rodriguez E, Morrow R, Mognard N, Lambin J, Vaze P, Lafon T (2010) The SWOT (Surface Water and Ocean Topography) Mission: Spaceborne Radar Interferometry for Oceanographic and Hydrological Applications. In: Hall J, Harrison DE, Stammer D (eds) Proceedings of the "OceanObs'09: Sustained Ocean Observations and Information for Society" Conference (Vol. 2), Venice, Italy, 21–25 September 2009, ESA Publication WPP-306

26. Fu L-L, Douglas A, Rodriguez E, Morrow R, Mognard N, Lambin J, Vaze P, Lafon T (2009) The SWOT (Surface Water and Ocean Topography) Mission: Spaceborne Radar Interferometry for Oceanographic and Hydrological Applications. In Proceedings of OceanObs'09, Venice, Italy, Sept. 21–25, 2009

27. Gleason ST, Adjrad M (2005) An Attempt to Sense Ocean Winds and Waves Empirically Using Bistatic GNSS Reflections in Low Earth Orbit. In Proceedings of the IEEE International Geosci and Rem Sens Symposium , Seoul, South Korea, 25–29 July 2005

28. Gohil BS, Sarkar A, Agarwal VK (2008) A new algorithm for wind vector retrieval from scatterometer. IEEE Geosci Rem Sens Letts 5:387–391

29. Gohil BS, Sharma P, Shikhakoli R, Sarkar A (2010) Directional stability and conservation of scattering (DiSCS) based directional-ambiguity removal algorithm for improving wind-fields from scatterometer: a QuikSCAT example. IEEE Geosci Rem Sens Letts 7:592–595

30. Gommenginger C et al (2011) Retracking altimeter waveforms near the coasts. In: Vignudelli S, Kostianoy A, Cipollini P, Benveniste J (eds) Coastal altimetry. Springer, Berlin Heidelberg, pp 61–102

31. Goni G et al (2010) The Ocean Observing System for Tropical Cyclone Intensification Forecasts and Studies. In: Hall J, Harrison DE, Stammer D (eds) Proceedings of the "OceanObs'09: Sustained Ocean Observations and Information for Society" Conference (Vol. 2), Venice, Italy, 21-25 September 2009, ESA Publication WPP-306

32. Guo JY, Hwang CW, Chang XT, Liu YT (2006) Improved threshold retracker for satellite altimeter waveform retracking over coastal sea. Prog Nat Sci 16:732–738

33. Halimi A, Mailhes C, Tourneret J-Y, Thibaut P, Boy F (2013) Parameter estimation for peaky altimetric waveforms. IEEE Trans Geosci Rem Sens 51:1568–1577

34. Hasselmann K et al (1985) Theory of synthetic aperture radar ocean imaging: a MARSEN view. J Geophys Res (Oceans) 90(C3):4659–4686

35. He R, Weisberg RH, Zhang H, Muller-Karger FE, Helber RW (2003) A cloud-free, satellite-derived, sea surface temperature analysis for the West Florida Shelf. Geophys Res Lett 30(15):1811. https://doi.org/10.1029/2003GL017673

36. Hersbach H, Stoffelen A, Haan De S (2007) An improved C-band scatterometer ocean geophysical model function: CMOD5. J Geophys Res 112:1–18. https://doi.org/10.1029/2006JC003743

37. Horstmann J, Koch W, Lehner S, Tonboe R (2000) Wind retrieval over the ocean using synthetic aperture radar with C-band HH polarization. IEEE Trans Geosci Remote Sens 38:2122–2131

38. Jackson CR, Apel JR (2004) Synthetic aperture radar marine user's manual. US Department of Commerce, National Oceanic and Atmospheric Administration, National Environmental Satellite, Data, and Information Serve, Office of Research and Applications

39. Ji M, Reynolds RW, Behringer DW (2000) Use of Topex/Poseidon sea level data for ocean analyses and ENSO prediction: some early results. J Clim 13:216–231
40. Kerr YH, Waldteufel P, Wigneron J-P, Martinuzzi J-M, Font J, Berger M (2001) Soil moisture retrieval from space: The Soil Moisture and Ocean Salinity (SMOS) mission. IEEE Trans Geosci Rem Sens 39:1729–1735
41. Koblinsky C, Gaspar P, Lagerloef G (eds) (1992) The future of spaceborne altimetry – oceans and climate change: a long-term strategy. Joint Oceanographic Institutions, Inc., 85 pp
42. Krishna Rao P, Smith WL, Koffler R (1972) Global sea-surface temperature distribution determined from an environmental satellite. Mon Weather Rev 100(1):10–14
43. Kumar R, Sarkar A, Pandey PC (1999) Estimation of ocean depths off Goa coast using ERS-1 Synthetic Aperture Radar. Cont Shelf Res 19(2):171–181
44. Kumar R, Chakraborty A, Parekh A, Shikakolli R, Gohil BS, Kiran Kumar AS (2013) Evaluation of Oceansat-2 derived ocean surface winds using observations from global buoys and other scatterometers. IEEE TGRS 51(5):2571–2576
45. Lagerloef GSE (2002) Introduction to the special section: the role of surface salinity on upper ocean dynamics, air sea interaction and climate. J Geophys Res 107(C12):8000. https://doi.org/10.1029/2002JC001669
46. Martin TV, Zwally HL, Brenner AC, Bindschadler RA (1983) Analysis and retracking of continental ice sheet radar altimeter waveform. J Geophys Res 88:1608–1616
47. Maus S, Green CM, Fairhead JD (1998) Improved ocean-geoid resolution from retracked ERS-1 satellite altimeter waveforms. Geophys J Int 134:243–253
48. McPhaden MJ, Delcroix T, Hanawa K, Kuroda Y, Meyers G, Picaut J, Swenson M (2001) The El Nino/Southern Osclillation (ENSO) observing system, in Observing the Ocean in the 21st Century. In Aust. Bur. of Meteorol., Melbourne, Victoria, Australia, 17 pp
49. Meissner T, Wentz FJ, Scott J (2015) Remote Sensing Systems SMAP level 3 Ocean Surface Salinities [Running 8-day, Monthly] on 0.25 deg grid, version 1.0 (BETA). www.remss.com/missions/smap
50. Mouche AA, Hauser D, Daloze JF, Guerin C (2005) Dual polarization measurements at C-band over the oceans: results from airborne radar observations and comparison with ENVISAT ASAR data. IEEE Trans Geosci Remote Sensing 43:753–769
51. Murtugudde R, Busalacchi AJ (1998) Salinity effects in a tropical ocean model. J Geophys Res 103:3283–3300
52. Pascual A, Faugère Y, Larnicol G, LeTraon P-T (2006) Improved description of the ocean mesoscalr variability by combining four satellite altimeters. Geophys Res Letts 33(2):13–16
53. Plant WJ (1997) A model for microwave Doppler sea return at high incidence angles: Bragg scattering from bound, tilted waves. J Geophys Res 102:21131–21146
54. Prigent C, Aires F, Bernardo F, Orlhac J-C, Goutoule J-M, Roquet H, Donlon C (2013) Analysis of the potential and limitations of microwave radiometry for the retrieval of sea surface temperature: definition of MICROWAT, a new mission concept. J Geophys Res Oceans 118:3074–3086
55. Ratheesh S, Mankad B, Basu S, Sharma R (2013) Assessment of satellite-derived sea surface salinity in the Indian Ocean. IEEE Geosci Rem Sens Lett 10(3):428–431. https://doi.org/10.1109/LGRS.2012.2207943
56. Ratheesh S, Sharma R, Sikhakolli R, Kumar R, Basu S (2014) Assessing sea surface salinity derived by Aquarius in the Indian Ocean. IEEE Geosci Rem Sens Letts 11:719722
57. Robinson IS (2005) Measuring the oceans from space. Praxis Publishing, Chinchester, 655 pp
58. Rodriguez E (1988) Altimetry for non-Gaussian oceans: Height biases and estimation of parameters. J Geophys Res 93:14107–14120
59. Sandwell DT, Smith WHF (2005) Retracking ERS-1 altimeter waveforms for optimal gravity field recovery. J Geophys Res 163:79–89
60. Schuchman RA, Lyzenga DR, Meadows GA (1985) Synthetic aperture radar imaging of ocean-bottom topography via tidal-current interactions: theory and observations. Int J Rem Sens 6:1179–1200

61. Severini J, Mailhes C, Tourneret J-Y, Thibaut P (2008) Bayesian estimation of altimeter echo parameters. In Proc. IEEE IGARSS, Boston, MA 3, pp III-238–III-241
62. Sharma R, Agarwal N, Momin IM, Basu S, Agarwal VK (2010) Simulated sea surface salinity variability in the Tropical Indian Ocean. J Clim 23:6542–6554
63. Steunou N, Desjonqueres JD, Picot N, Sengenes P, Noubel J, Poisson JC (2015) AltiKa Altimeter: instrument description and in flight performance. Mar Geod 38(S1):22–42
64. Stocker TF et al (2013) Technical Summary. In: Climate Change 2013: The Physical Science Basis. Contribution of Working Group I to the Fifth Assessment Report of the Intergovernmental Panel on Climate Change [Stocker, T.F., D. Qin, G.-K.Plattner, M.Tignor, S.K. Allen, J. Boschung, A. Nauels, Y. Xia, V. Bex andP.M. Midgley (eds.)]. Cambridge University Press, Cambridge, UK and New York, pp 33–115, doi:https://doi.org/10.1017/CBO9781107415324.005
65. Ulaby FT, Moore RK, Fung AK (1986) Microwave remote sensing: active and passive, Voll III: Volume scattering and emission theory, advanced systems and applications. Artech House Inc., Dedham, 1100 pp
66. Vincent P, Steunou N, Caubet E, Phalippou L, Rey L, Thouvenot E, Verron J (2006) AltiKa: A Ka-band altime-try payload and system for operational altimetry during the GMES period. Sensors 6:208–234
67. Vogelzang J (1989) A comparison of the hydrodynamic modulation in some existing models. Int J Rem Sens 10(9):1503–1518
68. Wijesekera HW et al (2016) ASIRI: an ocean atmosphere initiative for Bay of Bengal. Bull Amer Meteor Soc 97:1859–1884. https://doi.org/10.1175/BAMD-D-14-00197.1
69. Willis JK, Chambers DP, Kuo C-Y, Shum CK (2010) Global sea level rise: recent progress and challenges for the decade to come. Oceanography 23(4):26–35. https://doi.org/10.5670/oceanog.2010.03
70. Wilson S and Co-authors (2010) The Ocean Surface Topography Constellation: The Next 15 Years in Satellite Altimetry. In: Hall J, Harrison DE, Stammer D (eds) Proceedings of OceanObs'09: Sustained Ocean Observations and Information for Society (Vol. 2), Venice, Italy, 21–25 September 2009, ESA Publication WPP-306, doi:https://doi.org/10.5270/OceanObs09.cwp.92
71. Wingham DJ, Rapley CG, Griffiths HJ (1986) New technique in satellite altimeter tracking systems. IEEE-IGARSS 1:185–190
72. Yu L, McPhaden MJ (2011) Ocean preconditioning of cyclone Nargis in the bay of bengal: interaction between rossby waves, surface fresh waters, and sea surface temperatures. J Phys Oceanogr 41(9):1741–1755
73. Zavorotny VU, Voronovich AG (2000) Scattering of GPS signals from the ocean with wind remote sensing application. IEEE Trans Geosci Rem Sens 38:951–964